ELSEVIER

Sensors and Actuators A 102 (2002) 49–60

SENSORS AND ACTUATORS A PHYSICAL

www.elsevier.com/locate/sna

A high-aspect-ratio two-axis electrostatic microactuator with extended travel range

Yu Sun*, D. Piyabongkarn, A. Sezen, B.J. Nelson, R. Rajamani

Department of Mechanical Engineering, University of Minnesota, 111 Church Street S.E., Minneapolis, MN 55455, USA

Received 17 April 2002; received in revised form 22 July 2002; accepted 26 July 2002

Abstract

The design, fabrication, modelling, and control of a two-axis electrostatic microactuator for precision manipulation tasks is described. A high-yield fabrication process using deep reactive ion etching (DRIE) on silicon-on-insulator (SOI) wafers forms the 3-D high aspect ratio transverse comb drives that produce a relatively large electrostatic force. The structure is suspended by removing the substrate beneath the comb drives, therefore, a ground plane is not needed in order to compensate for electrostatic levitation. Among other advantages of the developed process is a dice-free release of wafer structures, allowing fragile structures to be individually packaged. Notching or footing effects and bowing effects are well-known problems in DRIE on SOI wafers. Techniques to overcome notching and bowing effects using a PlasmaTherm SLR-770 etcher are presented that do not require hardware modifications. A capacitive position sensing mechanism, capable of measuring displacements up to 4.5 μm with a resolution of 0.01 μm in both X and Y is integrated to provide position feedback. A nonlinear model inversion technique is proposed for nonlinear electrostatic microactuation system identification and improving system linearity and response. Pull-in instability limits the travel distance of transverse comb drive actuators. Using a nonlinear model inversion technique, a stable travel distance of 3.7 μm with a 4.5 μm gap has been achieved.
© 2002 Elsevier Science B.V. All rights reserved.

Keywords: DRIE; SOI; Electrostatic actuation; Microactuator; Nonlinear control

1. Introduction

Many microrobotic applications require multi-degree-of-freedom positioning at micro and nanoscales. Actuation technologies capable of providing motion at this scale include piezoactuators [1], microstepping motors [2], highly geared electromagnetic servomotors [3], and Lorentz force-type actuators such as voice coil motors [4]. Typically these positioning systems are expensive and require extensive calibration procedures. This paper reports on a newly developed novel electrostatic MicroElectroMechanical System (MEMS) microactuation system capable of two-axis positioning. The microactuator is designed for the manipulation of subcellular structures within biological cells [5], manipulation of large molecules such as DNA or proteins, and microassembly of hybrid MEMS devices.

Electrostatic comb-drive microactuators are established MEMS devices for positioning in the micron range [6,7]. A two-axis microactuator design was reported in [6]. X–Y microstages have been demonstrated for atomic force microscopy (AFM) applications [8,9]. Due to the high aspect ratio and the transverse movement of the comb drives, the two-axis electrostatic microactuator presented in this paper is capable of producing two orders of magnitude larger electrostatic forces than lateral comb drive microactuators while the required actuation voltages are approximately 10 times smaller. Another advantage of this device is that it is immune from levitation and does not require a ground plane.

Successful electrostatic actuation of micromechanical structures typically requires a ground plane under the structure in order to shield it from relatively large vertical fields. Without a properly designed ground plane, a microactuator is not capable of producing the desired motion due to the levitation effect [7], i.e. an unbalanced electrostatic field distribution making the structure move out of the actuation plane. However, the ground plane adds extra complexity in design and fabrication. By eliminating the ground plane and removing the substrate beneath the comb drive structure, this reported microactuator is ground plane free and immune from levitation because of the resulting balanced field distribution.

Polysilicon surface micromachining has been widely used to form interdigitated comb drive structures. The thinness of

* Corresponding author. Tel.: +1-612-6269104; fax: +1-612-6254344.
E-mail address: yus@me.umn.edu (Y. Sun).

0924-4247/02/$ – see front matter © 2002 Elsevier Science B.V. All rights reserved.
PII: S0924-4247(02)00298-4

the deposited polysilicon film limits several aspects of device performance, such as capacitive sensing sensitivity and electrostatic force output because of the small overlapping area between each pair of parallel plates [7,10–13]. Devices having comb finger depths of more than 12 μm only by using surface micromachining have not been reported. In addition, the use of polysilicon creates material and fabrication issues that do not appear in bulk micromachining processes such as residual stress, stress gradient through the film, variation of Young's modulus, topography variations with multiple-layer structures, and stiction [13]. To overcome these limitations, many processes have been developed and successfully adopted to form high aspect ratio comb drive structures including the SCREAM process [14,15], the dissolved wafer process [11], the etch-diffusion process [16], the surface/bulk micromachining process [17,18] and moulding processes such as LIGA [19] and HEXSIL [20].

This paper reports on a high yield process using deep reactive ion etching (DRIE) on silicon-on-insulator (SOI) to form high aspect ratio suspending interdigitated comb drive structures. The comb fingers are 50 μm in depth, greatly increasing capacitive position sensitivity and electrostatic force output and reducing the required actuation voltages because of the large overlapping area. An aspect ratio of more than 100 can be achieved using the developed process, which is a dice-free release of wafer structures, allowing fragile structures to be individually packaged. A yield of 86.4% has been achieved without significant process optimisation. Though bulk micromachining does not have the inherent surface micromachining problems such as stiction, DRIE on silicon-on-insulator (SOI) wafers demonstrates two well-known phenomena, notching or footing effects and bowing effects [21–25]. In this paper, techniques are described that overcome these effects.

To further improve the capacitive position sensitivity and produce large electrostatic forces, transverse movement of the movable plates is adopted instead of a lateral movement [7,10–13]. A lateral movement of plates changes the overlapping area of a parallel plate capacitor. The main advantage of using a lateral movement is the achievement of linearity between area change and capacitance change. However, the force output using the lateral movement mode is two orders of magnitude smaller than that using the transverse movement mode. The capacitive sensing of this microactuation system is also based on transverse movement of the movable plates rather than lateral movement. This gap change between plates provides higher position sensitivity and generates larger electrostatic force. The linear relationship between the gap change and capacitance change is maintained for small displacements.

When a microactuation system is used in micromanipulation, such as microrobotic surgery or cell manipulation [5], precise positioning is required and an overdamped system response is desired. However, nonlinearity is inherent in electrostatic microactuation systems and silicon microstructures are highly underdamped, which makes the control task difficult using traditional linear control methodologies. To compensate for system nonlinearity and obtain the desired system response, a nonlinear model inversion technique is used. Tracking control has been conducted to demonstrate the effectiveness of the technique.

Pull-in instability limits the travel distance of elastically suspended parallel-plate and transverse comb drive electrostatic microactuators to approximately $1/3$ of the undeflected gap distance. This instability is due to the electrostatic force increasing more rapidly than the spring force. It is desirable to increase the controllable travel range of an electrostatic microactuator beyond the $1/3$ limit for applications that require high fill factors. Several methods have been suggested to extend the controllable travel range by using a multiphase piecewise-linear mechanical flexure [26], by adding additional circuitry [27–29], by incorporating an on-board folded capacitor on the device [30], and by optimising the structural design [31]. A control law was proposed in [32] for linearising an electrostatic actuator, however, experimental results on fabricated devices were not reported. The first realistic design and analysis of device performance on a fabricated device were conducted by Chan and Dutton [30]. However, the scheme in [30] by incorporating an on-board capacitor not only requires additional device area, but also complicates the fabrication process. This paper presents experimental results using a nonlinear model inversion technique to extend the travel range to 3.7 μm without pull-in over a 4.5 μm gap. This approach to extending travel range does not require additional hardware and device area, and does not further complicate fabrication processes.

2. Electrostatic two-axis microactuator design

Fig. 1 shows the solid model of the microactuator design. The constrained outer frame and the inner movable plate are connected by four curved springs. When a voltage difference is applied on comb drives 1 and 4, the generated electrostatic force causes the movable plate to move in X, resulting in the movement of the manipulator for micromanipulation. This movement changes the gap between each pair of the parallel plates of comb drives 3 and 6 causing a capacitance change, which resolves the actuation motion. To create motion along Y, comb drive 2 and comb drive 5 are configured to be orthogonal to the comb drives in X. Note that the two comb drive capacitors located in the movable plate provide reference capacitance for the readout circuit and are not for actuation and sensing.

2.1. Actuation analysis

The offset comb drive model is shown in Fig. 2, where x is the displacement of the movable fingers from the equilibrium position. Based on the fundamental electrostatic force

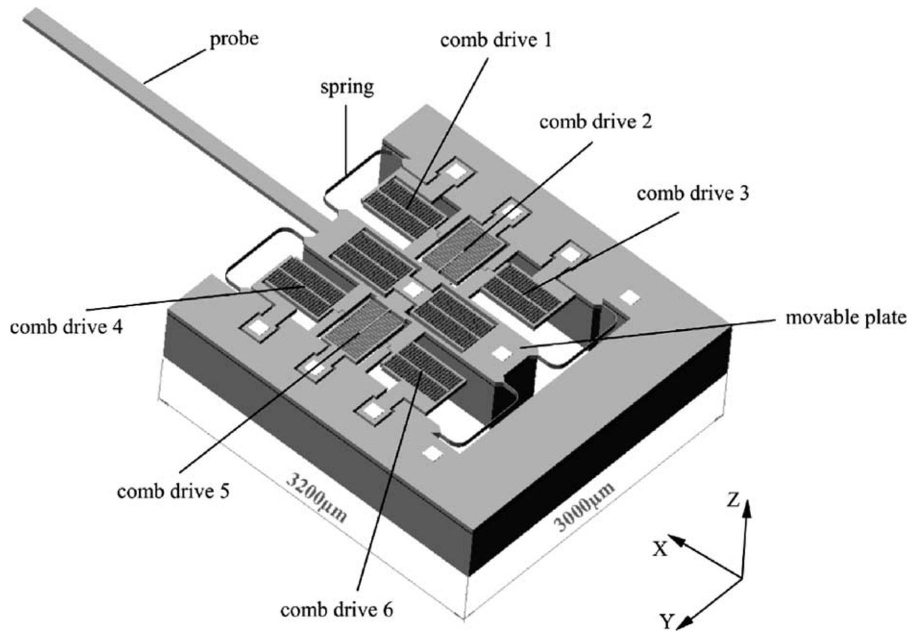

Fig. 1. Solid model of the two-axis microactuator.

equation [33], the force acting on the movable comb fingers is

$$F(x,V) = N(F_1 - F_2) = \frac{1}{2}N\left[\frac{\partial C_1}{\partial(x_1 - x)} - \frac{\partial C_2}{\partial(x_2 + x)}\right]V^2 = \frac{1}{2}NK\epsilon A\left[\frac{(x_1 + x_2)(x_2 - x_1 + 2x)}{(x_1 - x)^2(x_2 + x)^2}\right]V^2 \quad (1)$$

where N is the number of parallel capacitor pairs, K the dielectric constant for the material (for air $K = 1$), $\epsilon = 8.8542 \times 10^{-12}\,\mathrm{C^2/(N\,m^2)}$ is the permittivity of free space, $x_1 = 5\,\mu\mathrm{m}, x_2 = 12\,\mu\mathrm{m}, A = 7500\,\mu\mathrm{m}^2$ is the overlapping area of each finger pair, and V is the applied actuation voltage.

The dimensions of the springs shown in Fig. 1 determine the system stiffness. Structural analysis was performed numerically. The force-deflection model of the spring in both X and Y is

$$\delta = \lambda \frac{F}{Et^3h} \quad (2)$$

where δ is the deflection, F the force acting on the springs, $E = 125$ GPa the Young's modulus of silicon, $t = 7\,\mu\mathrm{m}$ the width of the springs and $h = 50\,\mu\mathrm{m}$ is the height of the springs. The values of λ are determined by simulation and are listed in Table 1.

The designed relationship between applied voltages and resulting motion in X and Y together with experimental calibration results are discussed in Section 4.2.

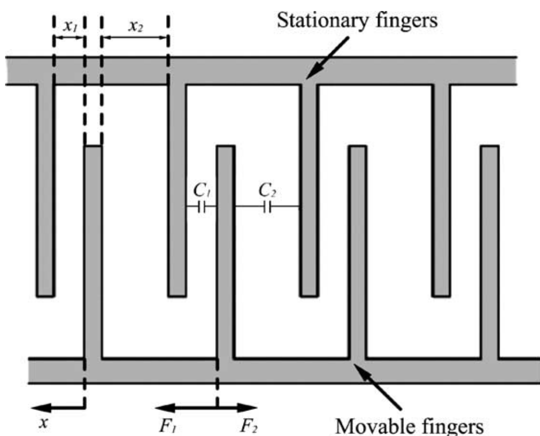

Fig. 2. Offset comb drive model.

2.2. Vertical levitation

Electrostatic microactuation typically requires a ground plane under the structure in order to shield the movable components from relatively large vertical fields. Without a ground plane, the application of a dc voltage will cause the structure to stick to the substrate. By directly placing a ground plane under the comb drives to prevent sticking, as shown in Fig. 3(a) where plates I and III are stationary and plate II is movable, the levitation effect [7] arises due to an unbalanced electric field distribution. This forces the structure to move out of the actuation plane. Electrostatic forces acting on the movable plate were determined numerically

Table 1
Values of λ in (2)

Design	λ in X (m^3)	λ in Y(m^3)
Curved springs	2.359×10^{-10}	1.101×10^{-11}

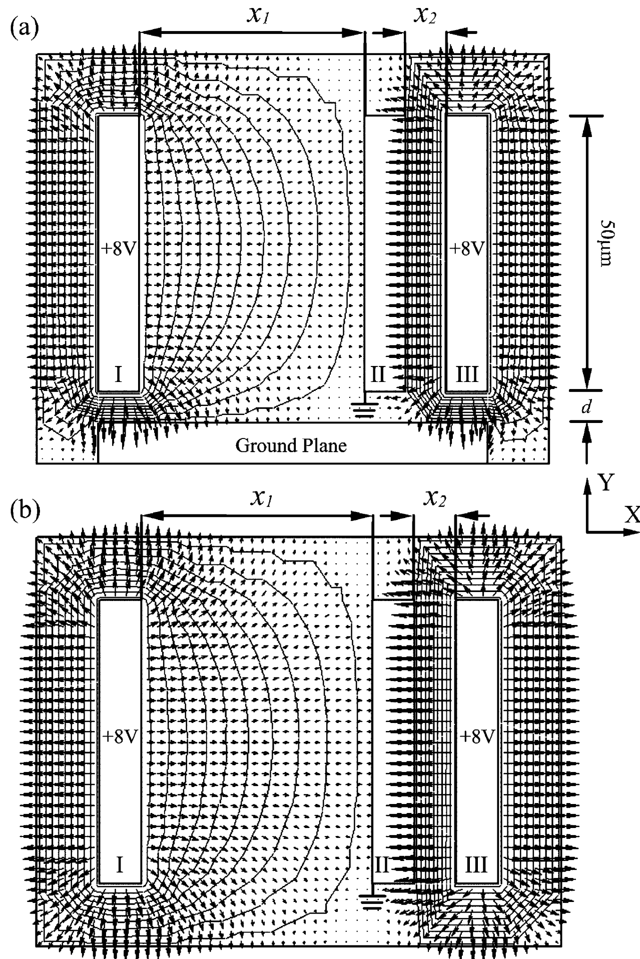

Fig. 3. Suspended comb drives avoid levitation; arrow: electric field; solid line: potential contour.

and are listed in Table 2 where F_Y is the vertical levitation force. To minimise the levitation effect, several methods have been proposed, such as using ground plane strips, cross-over structures and by applying differential dc bias [7]. However, these methods add further complexity in design and fabrication. The comb drives reported in this paper are suspended by completely removing the substrate beneath the comb drive structure. An electrostatic analysis demonstrates that making the comb drive structure suspended minimises the vertical levitation force. The micro-actuator is immune to levitation because of the resulting balanced field distribution shown in Fig. 3(b). Table 2 shows that the levitation forces are reduced by two orders of magnitude in the suspended comb drive design compared to the design with a ground plane shown in Fig. 3(a).

3. Fabrication

3.1. Fabrication sequence

Fabrication was conducted in the Microtechnology Laboratory at the University of Minnesota. The main processing steps are illustrated in Fig. 4.

(A) Start from a double polished P-type wafer with crystal orientation of ⟨1 0 0⟩.
(B) Low pressure chemical vapour deposition (LPCVD) 1 μm SiO_2.
(C) Fusion bond the wafer with SiO_2 with another P-type wafer.
(D) Chemical mechanical polishing (CMP) the top wafer down to 50 μm; this forms an SOI wafer.
(E) E-beam evaporate Al to form Ohmic contacts; Liftoff to pattern Al.
(F) Deep reactive ion etching (DRIE) to form the features on the back side such as the outer frame and movable plates. The buried 1 μm SiO_2 layer acts as an etch stop layer and also as an insulator between the capacitors.
(G) DRIE the top side to form capacitive comb fingers and curved springs. Thus, the comb drive structures are suspended.
(H) Reactive ion etching (RIE) to remove the buried SiO_2 layer; This releases the devices and ends the fabrication process. The dice-free release process protects fragile structures from being damaged. A yield of 86.4% has been achieved without significant process optimisation.

Wire bonding and packaging were undertaken, respectively, in the Microtechnology Laboratory and the Advanced Microsystems Laboratory. Fig. 5 shows the completed device.

3.2. DRIE on SOI wafers

The deep trench etcher used in the fabrication process is a PlasmaTherm SLR-770 Inductively Coupled Plasma Reactive Ion Etcher using the standard Bosch process. Passivation

Table 2
Electrostatic forces in X and Y

Design	x_1 (μm)	x_2 (μm)	F_X (N)	F_Y (N)	d (μm)
With ground plane	12	5	7.64×10^{-8}	8.18×10^{-9}	2
	14	3	2.44×10^{-7}	1.25×10^{-8}	2
Suspended comb drives	12	5	7.65×10^{-8}	9.97×10^{-11}	∞
	14	3	2.41×10^{-7}	1.14×10^{-10}	∞

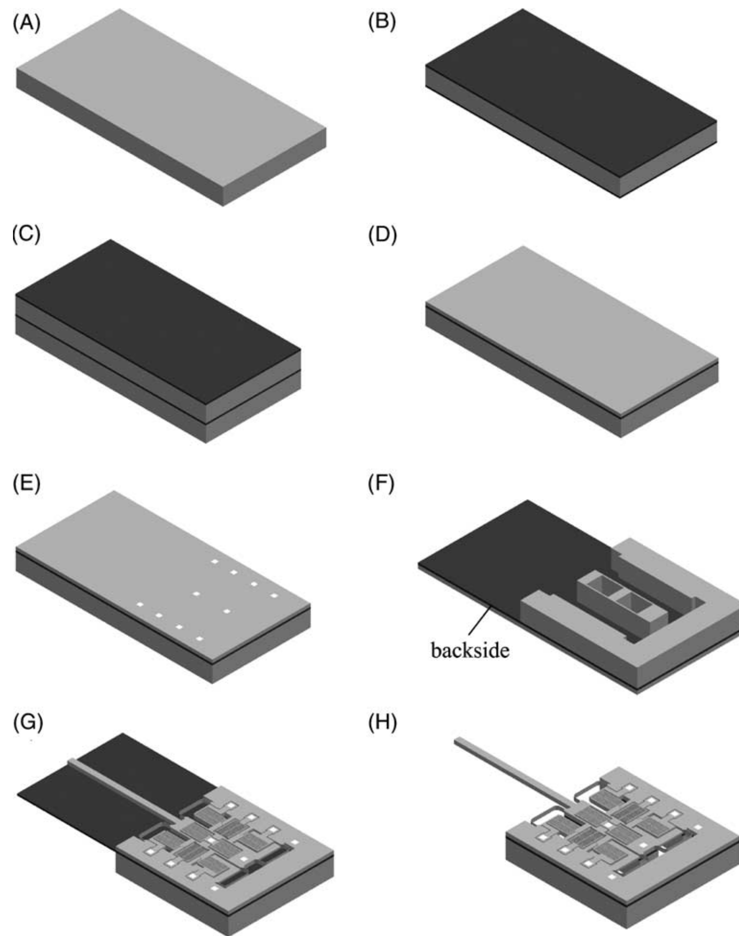

Fig. 4. Fabrication sequence.

is achieved by C_4F_8, and silicon etch by SF_6. In the beginning stage of processing, serious notching or footing effects arose due to the differential charging of sidewalls and bottoms of features [21–25]. Between the interface of Si and SiO_2, notching can extend laterally several microns. Another serious issue in DRIE on SOI experienced in the processing was the bowing effect [24] which makes etching near the mask opening isotropic. Fig. 6(a) shows that comb fingers of Si below the SiO_2 etch mask are undesirably removed because of the notching and bowing effects, causing the SiO_2 etch mask to float. The effects are more severe on small openings than on larger ones. Large openings have more free space for the ions to pass through without striking the sidewalls and are less sensitive to these effects. The notching effect has been theoretically investigated using the sheath model [21,23,25]. It has been proposed that to minimise these effects, one should design a mask having a uniform pattern width and large anchors that are tolerant of the notching and bowing. However, it is not always feasible to make the pattern sufficiently uniform in one design.

Recently, a DRIE tool from Surface Technology Systems integrates an additional low frequency RF power source

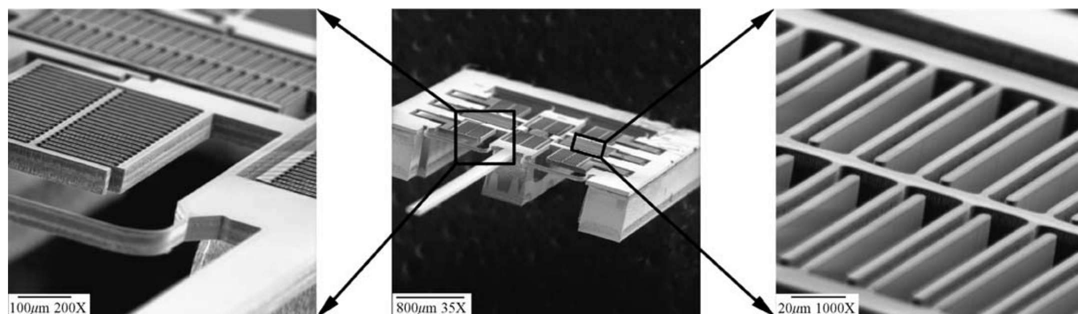

Fig. 5. SEM micrograph of the device.

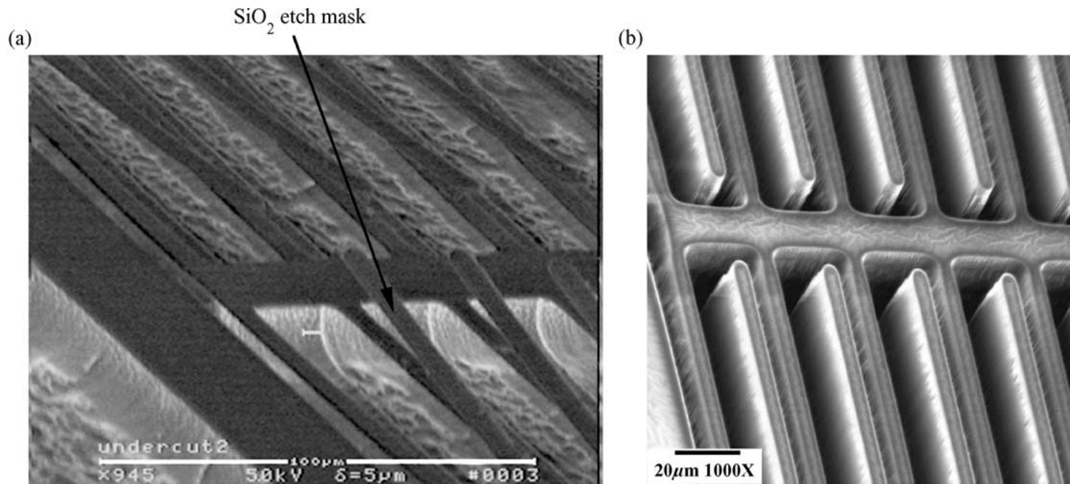

Fig. 6. Overcome the notching and bowing effects.

connected to a single-turn coil around the processing chamber. This essentially allows ions to escape more readily from deep trenches after the etching cycle, minimising notching and bowing effects. Even though this is encouraging for high aspect ratio etching in DRIE on SOI, it is not available for other existing DRIE equipment, such as the PlasmaTherm SLR-770.

In the investigation, three methods were used to significantly overcome notching and bowing effects. First, photoresist etch masks were used instead of SiO_2. It is well known that the selectivity of SiO_2 etch masks is high in DRIE. When SiO_2 etch mask is used, the localised chemistry of the plasma can be effected. The oxygen released by etching SiO_2 partially consumes the carbon from the C_4F_8 used for passivation, while a photoresist etch mask brings extra carbon into the local environment. Experimentation demonstrated that using photoresist etch masks significantly reduces notching and bowing effects than SiO_2 with the same flow rate of C_4F_8. Second, passivation effects were enhanced in the processing by lengthening passivation time and lowering etching power. Notching and bowing effects occur and are aggravated when the sidewall passivation polymer is removed faster than it forms. To achieve satisfactory passivation effects, it is desirable to either increase the flow rate of C_4F_8 or lengthen the time period of the passivation cycle in DRIE. In the processing, the passivation time was increased from 5 s as in the standard Bosch process to 6 s to enhance the passivation effects. The alternative method adopted to enhance the passivation effects was to lower the etching power in the etching cycle. The etching power was decreased from 9 to 7 W. This lowered etching power decreased the etch rate as expected. However, by lengthening the passivation cycle and decreasing the etching power, the bowing and notching effects were greatly reduced due to the enhanced passivation effects. Third, enhanced heat conduction was introduced into the etch process. The Bosch process for DRIE is sensitive to temperature change. When temperature increases, passivation effects deteriorate. Conversely, when temperature decreases, the efficiency of polymer deposition is increased while the etch rate is not greatly affected. Thus, varying chamber temperature can be an alternative way of controlling etch profile. It was determined that when heat from the ICP brings the wafer temperature over 100 °C, etching becomes isotropic. A heat conductive paste from AITechnology (Cool-grease 7016) was used to bond the device wafer to a carrier wafer instead of directly applying photoresist for bonding, which facilitated cooling from Helium on the chuck.

Combining the above three techniques, DRIE on SOI was successfully conducted. Features as small as 2 μm in the wafer plane survived the notching and bowing effects during the 50 μm vertical etching process as shown in Fig. 6(b).

4. System identification

4.1. System set-up

Fig. 7 shows the system set-up for system identification and real-time control. The xPC-Target1.3 from MathWorks was used to generate the real-time operating system kernel [34]. The capacitance readout circuitry consists of a microcontroller and a capacitive readout ASIC, the MS3110 from MicroSensors with a resolution of $4.0\,\mathrm{aF}/\sqrt{\mathrm{Hz}}$. An I/O board (National Instrument PCI-MIO-16E-4) performs sampling at a frequency of 40 KHz.

4.2. System modelling

The microactuator is modelled individually in X and Y as two spring-mass-damper systems.

$$m\ddot{x} + 2\zeta_i\sqrt{k_i m}\dot{x} + k_i x = \frac{1}{2}N_i K\epsilon A\left[\frac{(x_1+x_2)(x_2-x_1+2x)}{(x_1-x)^2(x_2+x)^2}\right]V_i^2 \quad (3)$$

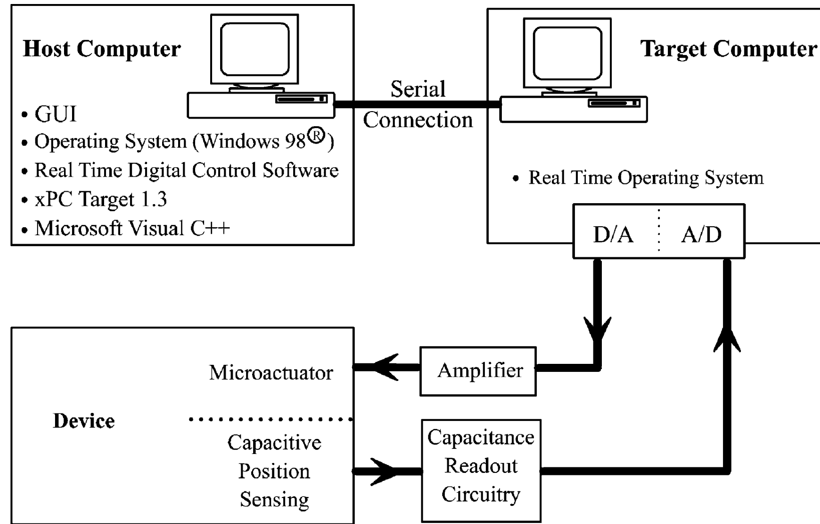

Fig. 7. Real-time control system set-up.

where $i = 1, 2$, m the equivalent concentrated mass, ζ the damping ratio, and k is the stiffness. The system consists of the linear equations of motion ($\text{EOM} = 1/m(s^2 + 2\zeta_i\omega_{ni}s + \omega_{ni}^2)$) and nonlinear electrostatic forces $F(x, V)$ given in (1).

The relationships between capacitance change for position sensing and actuation motion and between applied voltages and actuation motion were calibrated as shown in Figs. 8 and 9. The lower capacitive position sensitivity shown in Fig. 8 is mainly due to the parasitic capacitance in series with the sensing comb capacitors, such as occurs from poor Ohmic contact. Though the gap between the movable fingers and stationary fingers is set at 5μm, the full travel range is in effect 4.5 μm because of a mechanical amplitude limit designed into the device.

System stiffness in X and Y were determined statically from calibration results and verified using the system free response shown in Fig. 10. The identified system stiffness agrees well with the structural analysis results using finite element method. The underdamped free response in Fig. 10(a) and (b) was used to determine the damping ratio in X via [35]

$$\zeta = \frac{\delta}{\sqrt{4\pi^2 + \delta^2}} \tag{4}$$

where $\delta = \ln(B_1/B_2)$; B_1 and B_2 are the magnitude of two adjacent peaks. The estimated damping ratio in X is between 0.04 and 0.06. The natural frequency of the system in X using the relationship $\omega_d = \omega_n\sqrt{1 - \zeta^2}$, where ω_d is the damping frequency obtained from the free response, is

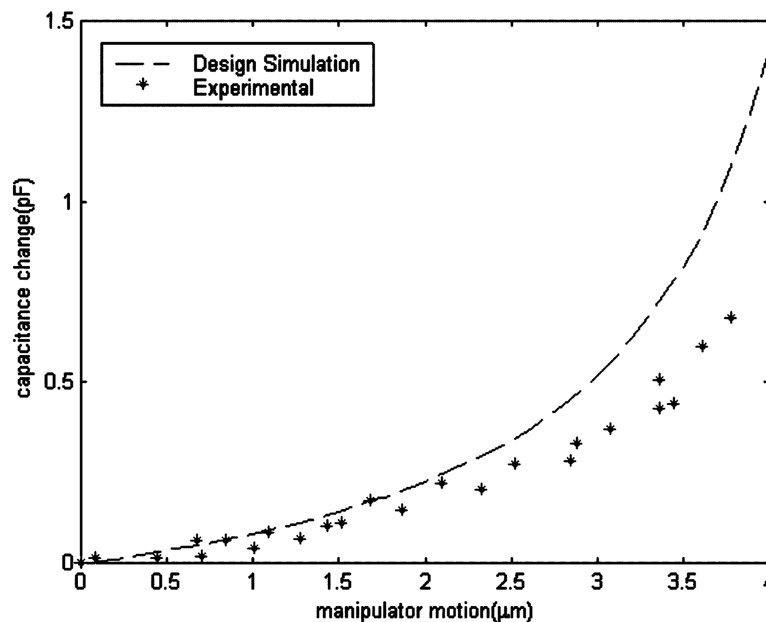

Fig. 8. Capacitive position sensing calibration.

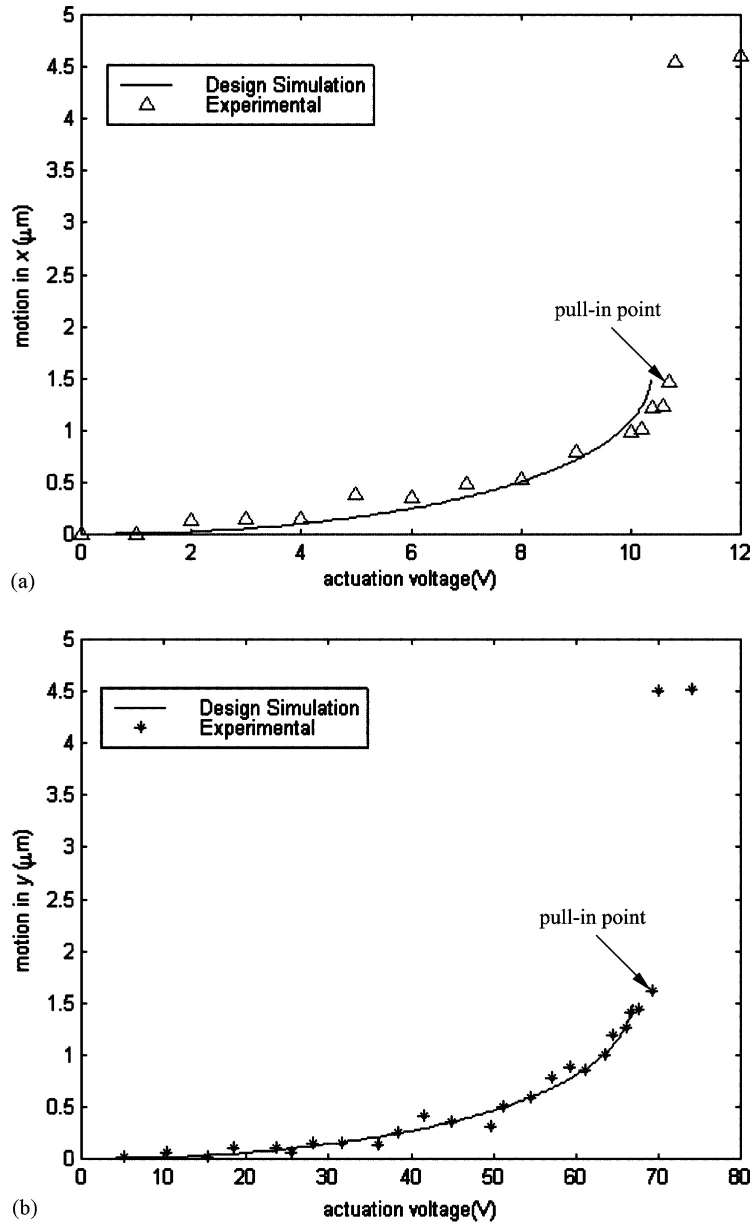

Fig. 9. Calibration of applied voltages and motion.

consistent with the result obtained using the identified system stiffness and the equivalent concentrated mass of the moving part using the relationship $\omega_n = (1/2\pi)\sqrt{k/m}$.

The free response reveals better linearity of the system in X, which is mainly due to the small actuation voltage range (less than 10.7 V) as shown in (1). In Y the system operates with actuation voltages up to 70 V, causing significant nonlinearity that can be seen in Fig. 10(c) and (d). A nonlinear model inversion technique is proposed to decouple the linear and nonlinear parts of nonlinear electrostatic microactuation systems for system identification and improvement of system response, which is discussed in Section 5. This technique was used for the identification of the EOM in Y. Table 3 shows the identified system parameters.

5. Tracking control

The nonlinear model inversion technique is shown in Fig. 11. The theoretical nonlinear model $F(x, V)$ and the inverse model $F^{-1}(x_{\text{meas}}, F_d)$ are

$$f(x, V) = \frac{1}{2}NK\epsilon A\left[\frac{(x_1 + x_2)(x_2 - x_1 + 2x)}{(x_1 - x)^2(x_2 + x)^2}\right]V^2,$$

$$f^{-1}(x_{\text{meas}}, F_d) = \sqrt{\frac{2F_d(x_1 - x_{\text{meas}})^2(x_2 + x_{\text{meas}})^2}{NK\epsilon A(x_1 + x_2)(x_2 - x_1 + 2x_{\text{meas}})}} \quad (5)$$

where x_{meas} is the position feedback from the capacitive position sensor; F_d is the control output from a linear

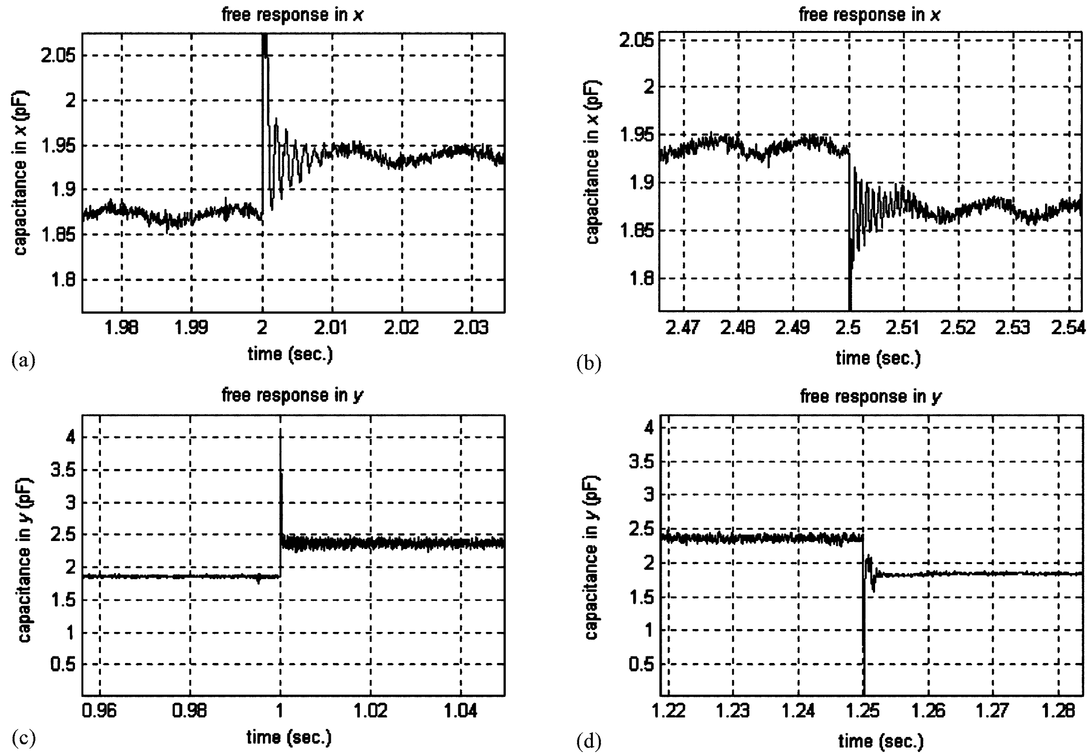

Fig. 10. Free responses of the system in X and Y.

Table 3
Identified system parameters

Parameter	System in X	System in Y
Mass, m (kg)	006.5×10^{-7}	0006.5×10^{-7}
Stiffness, k (μN/μm)	14.375	301.469
Natural frequency, ω_n (Hz)	748.46	3427.6
Damping ratio, ζ	[0.04, 0.06]	[0.12, 0.15]

controller, such as PID control. Using this technique allows for the use of traditional linear controller design methodologies for nonlinear electrostatic microactuation systems to obtain desired linear system response. For example, when the microactuation system is used in micromanipulation, such as microrobotic surgery or cell manipulation, an overdamped system response is desirable. This has been obtained using this nonlinear model inversion technique coupled with linear system controller design.

The other advantage of the proposed nonlinear model inversion technique is the increased tracking bandwidths in electrostatic microactuation systems. For a sinusoidal reference input, the tracking bandwidth was increased from 90 to 350 Hz in X and from 50 to 260 Hz in Y.

6. Pull-in extension

The net force on the movable fingers at voltage V and gap x is

$$F_{\text{net}} = \frac{1}{2} NK\epsilon A \left[\frac{(x_1 + x_2)(x_2 - x_1 + 2x)}{(x_1 - x)^2 (x_2 + x)^2} \right] V^2 - kx \qquad (6)$$

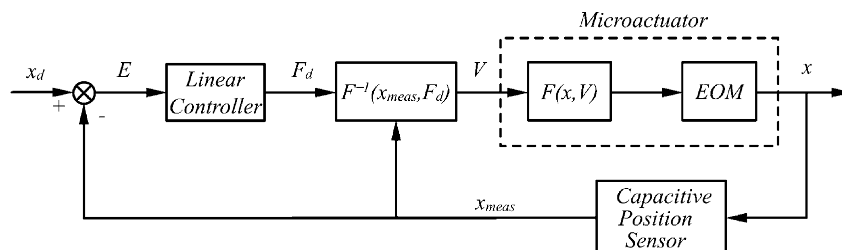

Fig. 11. Nonlinear model inversion position tracking.

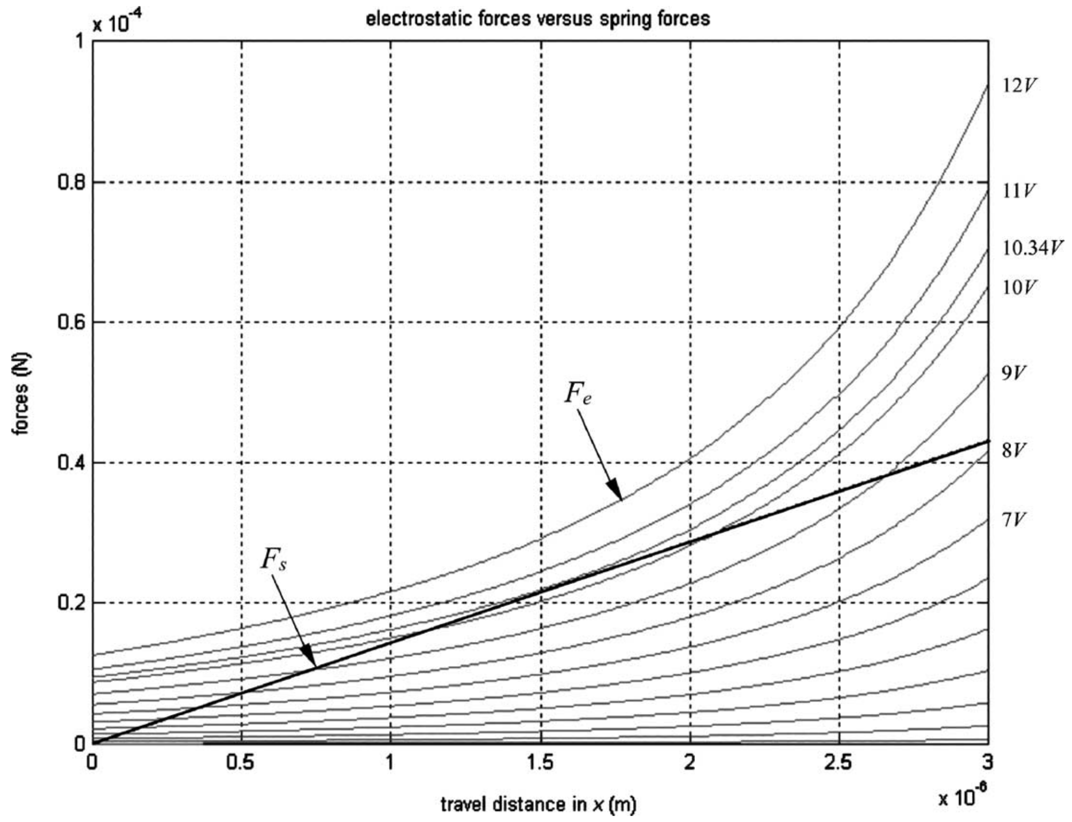

Fig. 12. Forces vs. travel distance in the X direction.

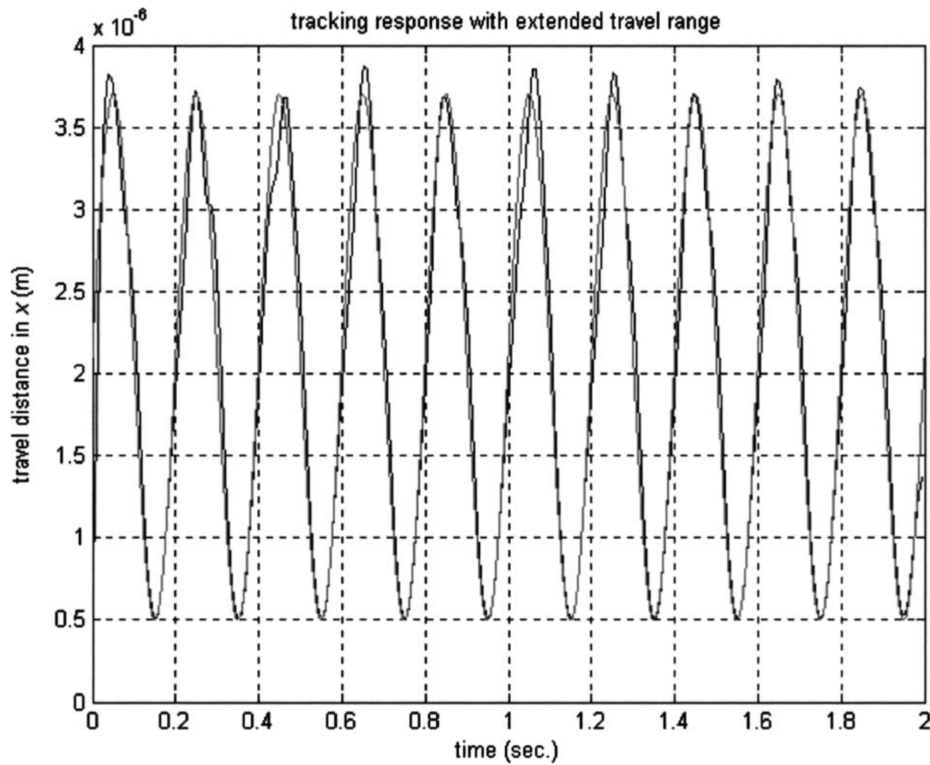

Fig. 13. Extended travel range tracking response.

To determine the stable equilibrium point x_{PI} and pull-in voltage V_{PI}, (6) is set to be zero and

$$k = NK\epsilon Af(x_1, x_2, x_{PI})V_{PI}^2,$$
$$f(x_1, x_2, x_{PI}) = \frac{(x_1 + x_2)[(x_2 - x_1 + 2x_{PI})^2 + (x_1 - x_{PI})(x_2 + x_{PI})]}{(x_1 - x_{PI})^3(x_2 + x_{PI})^3} \quad (7)$$

Fig. 12 shows that at the pull-in voltage $V_{PI} = 10.34$ V, the spring force F_s and electrostatic force F_e have only one intersection point. When a voltage larger than V_{PI} is supplied, the electrostatic force is larger than the spring force and the system becomes unstable. The stable travel distance x_{PI} is limited to 1.58 μm or 31.6% of the undeflected gap 5 μm.

To extend the stable travel range beyond the pull-in limit, the proposed nonlinear model inversion technique was used to increase system linearity. Consequently, a linear controller was designed for position tracking with an extended travel range as

$$\frac{F_d(s)}{E(s)} = K\frac{m(s^2 + 2\zeta\omega_n s + \omega_n^2)}{s(s+p)} \quad (8)$$

where K is the gain, and p represents the pole at high frequency. Because the designed controller cancels the $\text{EOM} = 1/m(s^2 + 2\zeta\omega_n s + \omega_n^2)$ dynamics, the loop transfer function operates as an integrator at low frequency having a cut-off frequency of approximately K/p. Due to the model uncertainty and low signal-to-noise ratio, the tracking bandwidth beyond the pull-in limit was limited to 120 Hz. The travel range was increased to 3.7 over 4.5 μm, extending the travel distance to 82.2% of the full range. The full travel range was not achieved due to the squeeze-film damping effect [32,36]. The sinusoidal tracking response with extended travel range is shown in Fig. 13.

7. Conclusions

This paper presents the design, fabrication, modelling, and control of a two-axis electrostatic microactuator. A high yield fabrication process using deep reactive ion etching (DRIE) on silicon-on-insulator (SOI) wafers forms the suspended 3-D high aspect ratio transverse comb drives, which produces high position sensitivity, large electrostatic forces and does not require the use of a ground plane for in-plane actuation. Notching or footing effects and bowing effects in DRIE on SOI wafers were investigated. Techniques to overcome notching and bowing effects using a PlasmaTherm SLR-770 etcher were presented that do not require hardware modifications. A nonlinear model inversion technique was proposed for nonlinear electrostatic microactuation system identification and improving system linearity and response. Using the proposed nonlinear model inversion technique, a stable travel distance of 3.7 over a 4.5 μm gap was achieved.

References

[1] N. Szita, R. Sutter, J. Dual, R.A. Buser, A micropipettor with integrated sensors, Sens. Actuators A 89 (1/2) (2001) 112–118.

[2] C.P. Navathe, B.L. Dashora, U.N. Roy, R. Singh, S. Maheswari, L.M. Kukreja, Control system for Langmuir–Blodgett film deposition set-up based on microstepping, Measure. Sci. Technol. 9 (3) (1998) 540–541.

[3] O. Barth, Harmonic piezodrive miniaturized servo motor, Mechatronics 10 (4/5) (2000) 545–554.

[4] A. Molenaar, E.H. Zaaijer, H.F. van Beek, A novel long stroke planar magnetic bearing actuator, in: Proceedings of the Fourth International Conference on Motion and Vibration Control, Zurich, Switzerland, August 1998, pp. 1071–1076.

[5] Y. Sun, B.J. Nelson, Microrobotic cell injection, in: Proceedings of the IEEE International Conference on Robotics and Automation, 2001, pp. 620–625.

[6] T. Harness, R.R.A. Syms, Characteristic modes of electrostatic comb-drive X–Y microactuators, J. Micromech. Microeng. 9 (1999) 1–8.

[7] W.C. Tang, M.G. Lim, R.T. Howe, Electrostatic comb drive levitation and control method, J. Microelectromech. Syst. 1 (4) (1992) 170–178.

[8] P.F. Indermuehle, C. Linder, J. Brugger, V.P. Jaecklin, N.F. de Rooij, Design and fabrication of and overhanging xy-microactuator with integrated tip for scanning surface profiling, Sens. Actuators A 43 (1994) 346–350.

[9] P.F. Indermuehle, V.P. Jaecklin, J. Brugger, C. Linder, N.F. de Rooij, AFM imaging with an xy-micropostioner with integrated tip, Sens. Actuators A 46/47 (1995) 562–565.

[10] T. Hirano, T. Furuhata, K.J. Gabriel, H. Fujita, Design, fabrication, and operation of submicron gap comb-drive microactuators, J. Microelectromech. Syst. 1 (1) (1992) 52–59.

[11] A.W. Selvakumar, K. Najafi, A high sensitivity Z-axis capacitive silicon microaccelerometer with a torsional suspension, J. Microelectromech. Syst. 7 (2) (1998) 192–200.

[12] W.C. Tang, T.H. Nguyen, M.W. Judy, R.T. Howe, Electrostatic-comb drive of lateral polysilicon resonators, Sens. Actuators A 21–23 (1990) 328–331.

[13] J.L.A. Yeh, H. Jiang, N.C. Tien, Integrated polysilicon and DRIE bulk silicon micromachining for an electrostatic torsional actuator, J. Microelectromech. Syst. 8 (4) (1999) 456–465.

[14] R. Prasad, N. MacDonald, D. Taylor, Micro-instrumentation for tribological measurement, in: Proceedings of the Eighth International Conference on Solid-State Sensors and Actuators, Sweden, 25–29 June 1995, pp. 52–55.

[15] Y. Xu, S.A. Miller, N.C. MacDonald, Microelectromechanical scanning tunneling microscope, in: Proceedings of the 8th International Conference on Solid-State Sensors and Actuators, 1995, pp. 640–643.

[16] W.H. Juan, S.W. Pang, Released Si Microstructures fabricated by deep etching and shallow diffusion, J. Microelectromech. Syst. 5 (1) (1996) 18–23.

[17] S. Lee, S. Park, D. Cho, The surface/bulk micromachining (SBM) process: a new method for fabricating released MEMS in single crystal silicon, J. Microelectromech. Syst. 8 (4) (1999) 409–416.

[18] S. Lee, S. Park, J. Kim, S. Lee, D. Cho, Surface/bulk micromachined single-crystalline-silicon micro-gyroscope, J. Microelectromech. Syst. 9 (4) (2000) 557–567.

[19] S. Takimoto, R. Kondo, K. Suzuki, S. Sugiyama, Fabrication of micromotors using LIGA process, in: Proceedings of the International Symposium on Micromechatronics and Human Science, 1999, pp. 221–226.

[20] D.A. Horsley, A. Singh, A.P. Pisano, R. Horowitz, Angular micropositioner for disk drives, in: Proceedings of the Tenth IEEE International Workshop on Micro Electro Mechanical Systems, 1997, pp. 454–459.

[21] J.C. Arnold, H.H. Sawin, Charging of pattern features during plasma etching, J. Appl. Phys. 70 (10) (1991) 5314–5317.
[22] A.A. Ayón, K. Ishihara, R.A. Braff, H.H. Sawin, M.A. Schmidt, Microfabrication and testing of suspended structures compatible with silicon-on-insulator technology, J. Vac. Sci. Technol. B 17 (4) (1999) 1589–1593.
[23] G.S. Hwang, K.P. Giapis, On the origin of the notching effect during etching in uniform high density plasmas, J. Vac. Sci. Technol. B 15 (1) (1997) 70–87.
[24] K. Ishihara, C.F. Yung, A.A. Ayón, M.A. Schmidt, An inertial sensor technology using DRIE and wafer bonding with interconnecting capability, J. Microelectromech. Syst. 8 (4) (1999) 403–408.
[25] T. Kinoshita, M. Hane, J.P. McVittie, Notching as an example of charging in uniform high density plasmas, J. Vac. Sci. Technol. B 14 (1) (1996) 560–565.
[26] D.M. Burns, V.M. Bright, Nonlinear flexture for stable deflection of an electrostatically actuated micromirror, in: Proceedings of the SPIE on Microelectronics Structures and MEMS for Optical Processing III, Vol. 3226, 1997, pp. 125–135.
[27] J.I. Seeger, S.B. Crary, Stabilization of electrostatically actuated mechanical devices, in: Proceedings of the Transducers, 1997, pp. 1133–1136.
[28] J.I. Seeger, S.B. Crary, Analysis and simulation of MOS capacitor feedback for stabilizing electrostatically actuated mechanical devices, in: Proceedings of the Microsim II on Comput. Mech., 1998, pp. 199–208.
[29] J.I. Seeger, B.E. Boser, Dynamics and control of parallel-plate actuators beyond the electrostatic instability, in: Proceedings of the Transducers, 1999, pp. 474–477.
[30] E.K. Chan, R.W. Dutton, Electrostatic micromechanical actuator with extended range of travel, J. Microelectromech. Syst. 9 (3) (1999) 321–328.
[31] E.S. Hung, S.D. Senturia, Extending the travel range of analog-tuned electrostatic actuators, J. Microelectromech. Syst. 8 (4) (1999) 497–505.
[32] P.B. Chu, K.S.J. Pister, Analysis of closed-loop control of parallel-plate electrostatic microgrippers, in: Proceedings of the IEEE International Conference on Robotics and Automation, 1994, pp. 820–825.
[33] A.D. Moore, Electrostatics and Its Applications, Wiley, New York, 1973.
[34] P.S. Shiakolas, D. Piyabongkarn, On the development of a real-time digital control system using xPC-Target and a magnetic levitation device, in: Proceedings of the 40th IEEE Conference on Decision and Control, 2001, pp. 1348–1353.
[35] W.J. Palm, Modeling, Analysis and Control of Dynamic Systems, Wiley, New York, 2000.
[36] W.S. Griffin, H.H. Richardson, S. Yamanami, A study of fluid squeeze-film damping, Transactions of the ASME, J. Basic Eng. (1966) 451–456.

Biographies

Yu Sun received the BS degree in Electrical Engineering from the Dalian University of Technology, China, in 1996, and the MS degree in Electrical Engineering from the Institute of Automation, Chinese Academy of Sciences, Beijing, China, in 1999. He is currently a PhD candidate in the Mechanical Engineering Department at the University of Minnesota. His research interests are in the areas of MEMS design, fabrication and testing, control of microstructures, microrobotics, and intelligent micromanipulation for biomedical applications.

D. Piyabongkarn received the B.Eng. degree in mechanical engineering from Chulalongkorn University, Bangkok, Thailand, in 1996, and the M.S. degree in Mechanical Engineering from the University of Texas at Arlington in 2000. He is currently pursuing his PhD in Mechanical Engineering at the University of Minnesota. His research interests include advanced controls, MEMS, microactuators, microgyroscopes, signal processing, and artificial neural networks.

A. Sezen received his B.S. and M.S. degrees in Mechanical Engineering from the Middle East Technical University, Turkey, in 1999 and 2001, respectively. He is currently pursuing his Ph.D. in Mechanical Engineering at the University of Minnesota. His research interests include MEMS design and manufacturing, kinematic design of mechanisms, compliant mechanisms, robotics and control.

B.J. Nelson is the Mayhugh associate professor of Mechanical Engineering at the University of Minnesota. He received the BS degree in Mechanical Engineering from the University of Illinois at Urbana-Champaign in 1984, the MS degree in Mechanical Engineering from the University of Minnesota in 1987, and the PhD degree in Robotics (School of Computer Science) from Carnegie Mellon University in 1995. He has been an assistant professor at the University of Illinois at Chicago, has worked as an engineer for Honeywell Inc. and Motorola Inc., and has served as a United States Peace Corps Volunteer in Botswana, Africa. He has been awarded a McKnight Land-Grant Professorship and is a recipient of the Office of Naval Research Young Investigator Award, the National Science Foundation Faculty Early Career Development (CAREER) Award, and the McKnight Presidential Fellows Award. At the University of Illinois he was awarded the Bronze Tablet, the highest award for academic achievement offered by this institution. His research interests include biomedical engineering, computer vision, controls, manufacturing, mechatronics, MEMS, microrobotics, robotics. His most recent scientific contributions have been in the area of microrobotics, including efforts in robotic micromanipulation, microassembly, MEMS, mechanical manipulation of biological cells and tissue, and nanofabrication.

R. Rajamani obtained his MS and PhD degrees from the University of California at Berkeley in 1991 and 1993, respectively, and his B.Tech degree from the Indian Institute of Technology at Madras in 1989. After obtaining his PhD, Dr. Rajamani spent 5 years working as a Research Engineer first at United Technologies Research Center (UTRC) and then at California PATH. Since September 1998, Dr. Rajamani has been Nelson assistant professor in the Department of Mechanical Engineering at the University of Minnesota. His active research interests include control design and state estimation for nonlinear systems, fault diagnostics, intelligent transportation systems, active noise control and MEMS sensor design. Dr. Rajamani has authored over 40 refereed publications and received two patents. He has won several awards including the CAREER award from the National Science Foundation, the 2001 Outstanding Paper award from the journal IEEE Transactions on Control Systems Technology, the Distinguished Service Team Award from the University of California, Berkeley and the Outstanding Achievement of the Year award from United Technologies Research Center.